Supplemental Material

Concerted mass transport governs anomalous diffusion in anharmonic bcc metals

Davide G. Sangiovanni,[1*] Carlos R. Salazar,[1] Ferenc Tasnádi,[1] Johan Klarbring,[1] Igor A. Abrikosov[1]

[1]Department of Physics, Chemistry, and Biology (IFM) Linköping University, SE-581 83, Linköping, Sweden

[*]Corresponding author: davide.sangiovanni@liu.se

S1. Equilibrium volumes in bcc Ti as a function of temperature

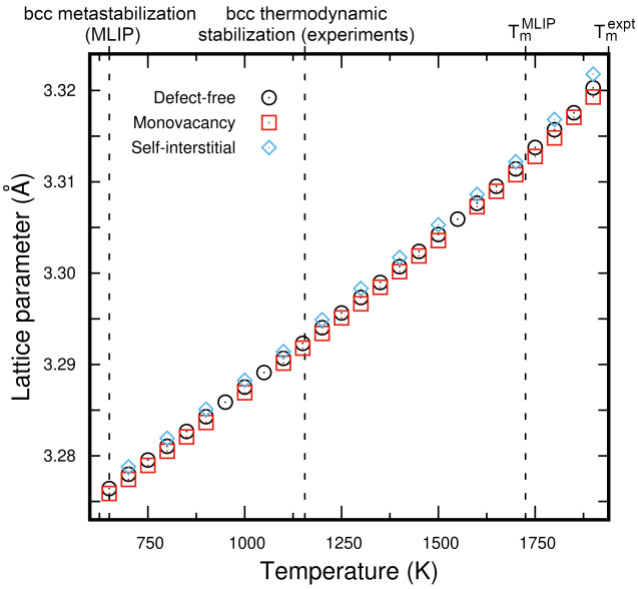

Figure S1. Lattice parameters of bcc titanium determined by NpT MLIP-MD simulations on 9 × 9 × 9 bcc supercells. The results are plotted for supercells initially free of defects or containing one vacancy or one self-interstitial. According to the MLIP used in this work, the bcc structure is meta-stabilized above ~650 K and melts at T_m^{MLIP}=1725±25 K (see **Fig. S6**). The experimental melting temperature T_m^{expt} is ~1940 K.

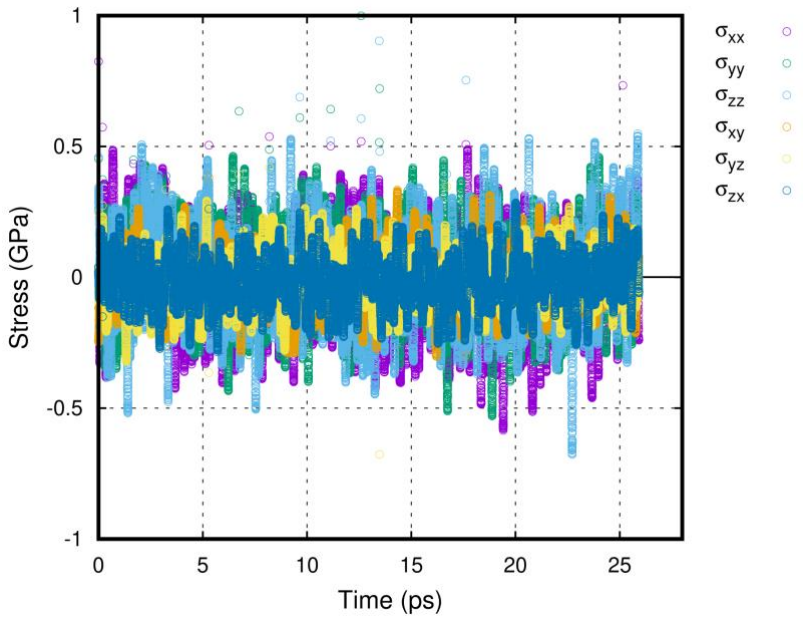

Figure S2. Post-equilibration AIMD stresses as a function of simulation time in bcc Ti supercells at T_{sim} near melting.

S2. Concerted migration induced by isolated point defects in bcc Ti

Figures S3 and S4 illustrate examples of highly correlated migration of native vacancy and self-interstitial (crowdion-like) defects in 3D periodic supercells of bcc Ti. In absence of diffusion reactions activated in defect-free regions, the native point defect is the only species that migrates during the simulation. The results of defect concentration-independent diffusivities $D^{\mathrm{V\,/\,SI}}_{\text{c-indep.}}$ (**Eq. 2** of the **main text**) remain invariant with increased supercell size as long as the model is large enough to accommodate all vibrational modes that significantly contribute to diffusion (see, for example, effects of surface vibration degrees of freedom on adatom migration in figure 5 of Ref. [1]). Preliminary simulation tests demonstrate that $D^{\mathrm{V\,/\,SI}}_{\text{c-indep.}}$ values computed for 6×6×6 bcc supercells at temperatures from 700 to 1200 K during 10 ns match (within error bars) with $D^{\mathrm{V\,/\,SI}}_{\text{c-indep.}}$ determined for 9×9×9 bcc supercells at the same temperatures. Within these timeframes and at temperatures above 1200 K, larger supercells are likely to activate concerted diffusion, which complicates isolating the individual contribution of vacancy migration.

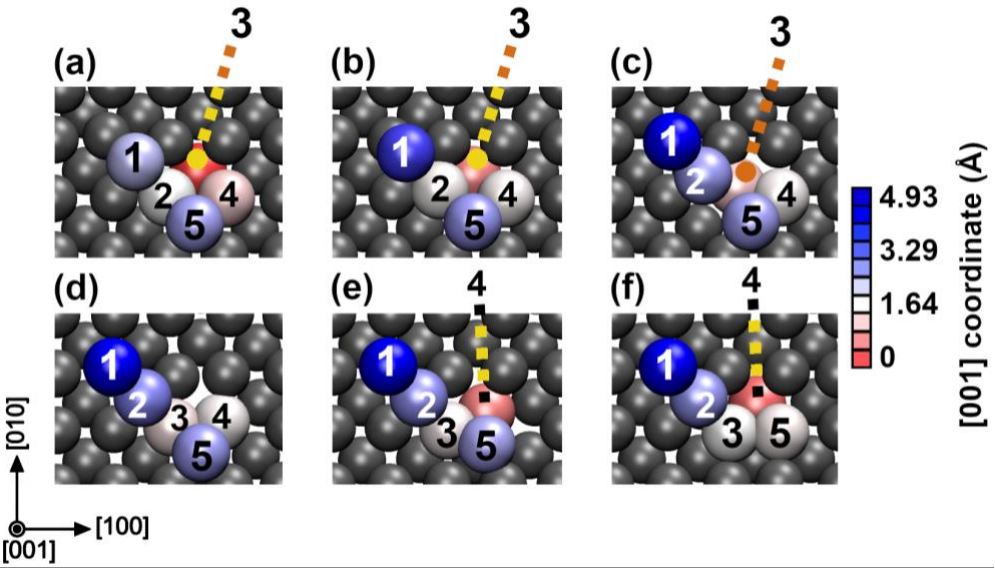

Figure S3. Monovacancy-driven concerted migration in bcc Ti at 900 K simulated by MLIP-MD using 9 × 9 × 9 bcc supercells. The timelapse between panels is ~2 ps (10 ps from **(a)** to **(f)**). Atoms on the string are numbered from #1 (leading) to #5 (trail). The atomic coordinates are time averaged to minimize thermal noise. **(a,b,c)** The reaction starts with atom#1 moving along $[\bar{1}11]$ to fill the lattice vacancy, concertedly followed by atom#2 which translates along $[\bar{1}11]$ to occupy atom's#1 site. **(b–f)** The translation of atoms#1 and #2 is readily accompanied by a synchronized rotation of the #3-#4-#5 triangle within the (011) plane. Effectively, atoms#3, #4, and #5 translate along $[\bar{1}\bar{1}1]$, $[\bar{1}1\bar{1}]$, and $[11\bar{1}]$. In each snapshot, the string atoms are colored according to their instantaneous [001] coordinate, orthogonal to the plane of view (see color legend). **(a)** Prior to migration, the string is comprised of four diatomic segments oriented as: #2→#1 // $[\bar{1}11]$; #3→#2 // $[\bar{1}\bar{1}1]$; #4→#3 // $[\bar{1}1\bar{1}]$; #5→#4 $[11\bar{1}]$. **(f)** Post-migration, the string segments are oriented as: #3→#2→#1 // $[\bar{1}11]$; #4→#3 // $[\bar{1}\bar{1}1]$; #5→#4 // $[\bar{1}1\bar{1}]$.

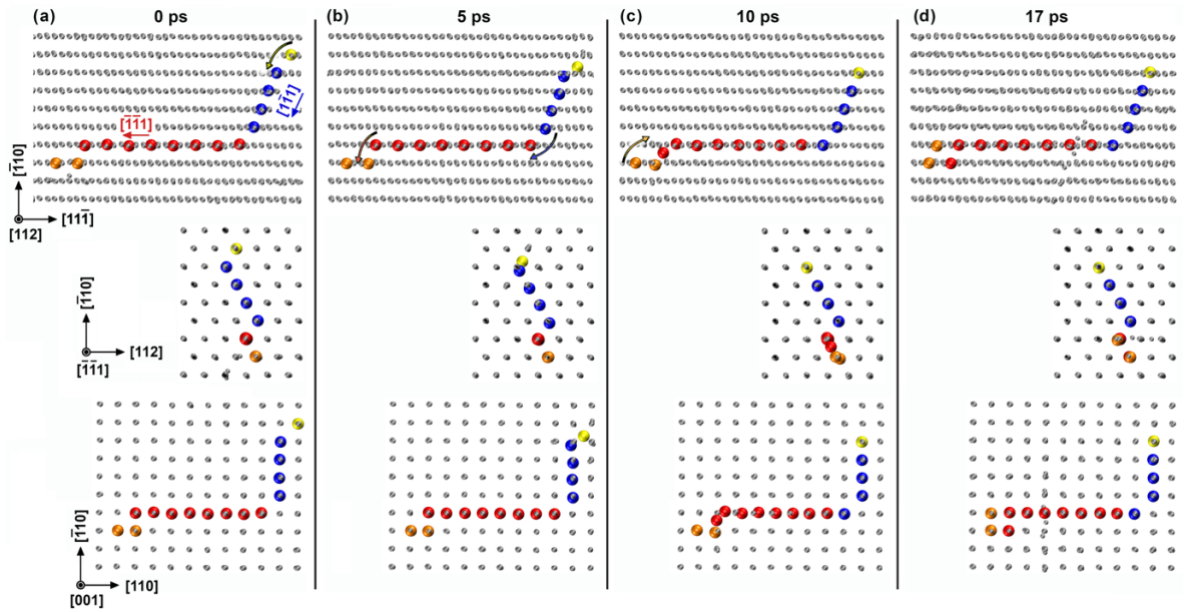

Figure S4. Self-interstitial migration in bcc Ti at 900 K modelled by MLIP-MD, using 9 × 9 × 9 bcc supercells. The mechanism is initiated with the yellow atom acting as self-interstitial defect that compresses a $[1\bar{1}1]$ lattice row (blue atoms). In the top panel **(a)**, the red atoms of the string move concertedly toward the left ($[\bar{1}\bar{1}1]$ direction). The red string segment is orthogonal to the direction of view. In the mid panels, the direction of view is parallel to the motion of the red string segment. In **(a)**, atoms colored in blue, red, and orange are segments of different ⟨111⟩ lattice rows. In the lower panels, the red string segment is inclined 35.26º to the (001) plane (i.e., forms an angle of 54.74º with the [001] direction of view).

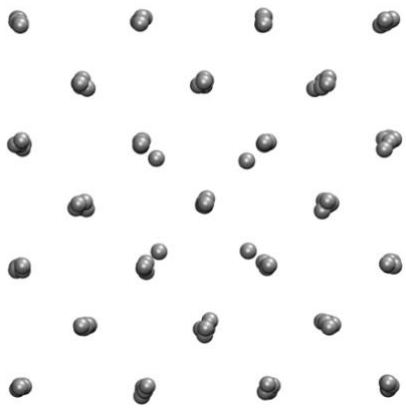

Figure S5. Time-averaged atomic positions in bcc Ti at 900 K near a vacancy site (center of the image). The vacancy neighbors are shifted approximately by ¼ of the interatomic distance d_{NN} toward the vacancy.

S3. High-temperature annealing of Ti(001) and W(001) surface-slab models

To determine the total diffusivity of bcc Ti, we first need to determine the equilibrium concentration of missing atoms $c_V^{MA}(T)$ – that is, the atom deficit in the bulk. That value is lower than the instantaneous total population of vacant lattice sites $c_V(T)$ due to "transient" vacancy–interstitial defects that rapidly form and annihilate in pristine (defect-free) crystal regions and contribute to the total $c_V(T)$. To this end, we anneal Ti and W surface-slab models by MLIP-MD simulations. The Ti and W slab models have (001) surface termination and contain 30×30×56 bcc cells (100800 atoms – smaller surface-slab) or 50 × 50 × 90 bcc cells (450000 atoms – larger surface-slab). Imposing lateral equilibrium distances of the 3D periodic crystal (see **Fig. S1**), the surface slabs are equilibrated in the NVT ensemble during ≥2 ns; time sufficient to achieve a steady defect concentration in the central 30 layers (or 58 layers for larger cells). For bcc Ti, the simulations are done at temperatures of 1200, 1300, 1400, 1500, 1600, 1700, 1750, and 1800 K. W is annealed at

3000 K. Note that the results are invariant of the surface-slab orientation and are saturated with respect to the size of the model [2].

Vacancy–adatom pair formation and vacancy migration in bcc W are relatively slow processes, even at a temperature of 3000 K. Hence, the W(001) surface-slab model is initialized directly with 9 vacancies randomly placed on the 100800 available bcc sites, yielding an initial defect concentration ($c_V^{initial} = 8.9 \cdot 10^{-5}$); within the range $[(8.3 \pm 1.3) \cdot 10^{-5}]$ calculated using **Eq. 4** in the **main text** with $G_V^f(3000\ K) = 2.43 \pm 0.04$ eV [3]. We assume validity of the DFT/PBE melting temperature $T_m = 3349$ K (~10% lower than $T_m^{expt} = 3695$ K); consistent with the PBE-based DFT data on which the MLIP of Ref. [4] was trained. MLIP-MD results show that bcc W(001) equilibrated at 3000 K retains a perfectly crystalline structure throughout the simulation (**Fig. S6f**).

For bcc Ti, we first assess melting within the MLIP framework (**Fig. S6**). The structure remains crystalline up to 1700 K, exhibiting only minor surface roughening due to adatom-vacancy exchange reactions. Annealing at 1750–1800 K leads to rapid proliferation of atomic chains, loss of crystalline order, and eventual melting, as seen in **Fig. S6b–e**. From this transition, we estimate an MLIP melting temperature of $T_m^{MLIP} \approx 1725 \pm 25$ K; ~11% below experiments.

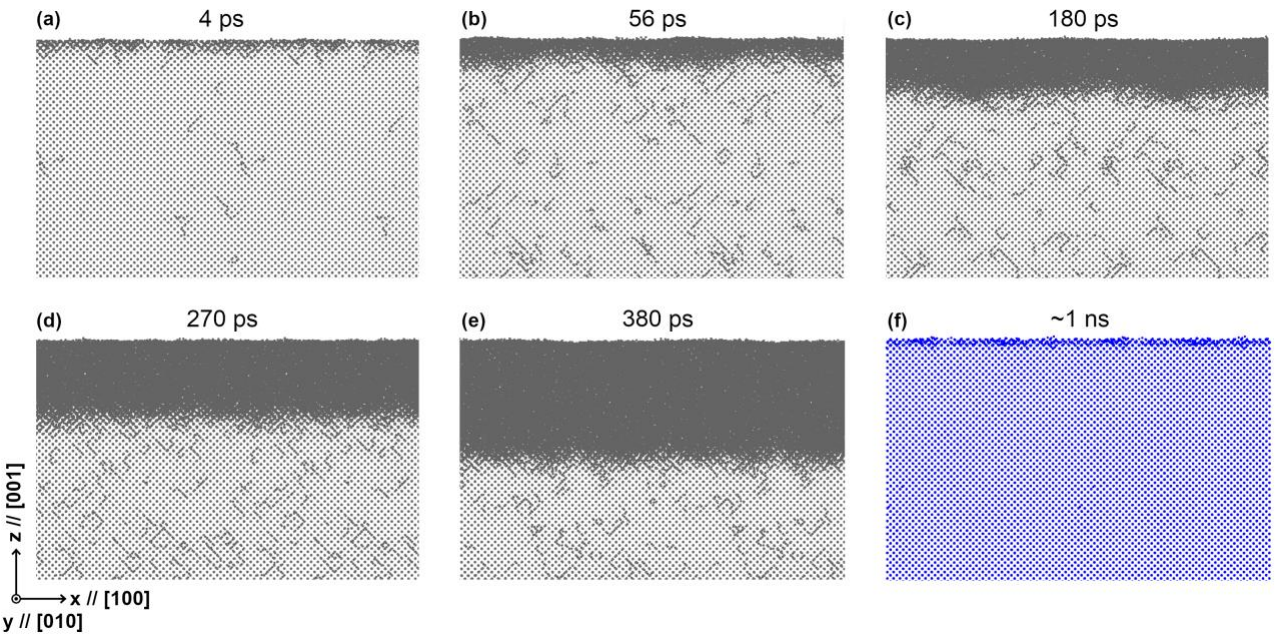

Figure S6. MLIP–MD simulation snapshots of surface-slab models (only top surfaces of smaller slabs are shown) annealed at elevated temperature. Atomic positions are time-averaged over 1 ps. At 1750 K, bcc Ti(001) progressively loses crystalline order, indicating surface-initiated melting **(a–e)**; by ~0.4 ns, roughly half of the slab has melted **(e)**. In contrast, bcc W(001) equilibrated at 3000 K remains fully solid **(f)**. For comparison, at 1700 K the Ti(001) slab retains its crystalline structure – apart from minor surface effects associated with adatom formation – and appears similar to panel **(a)** throughout the entire ~2 ns simulation. Based on these observations, we estimate an MLIP melting point for Ti of 1725±25 K.

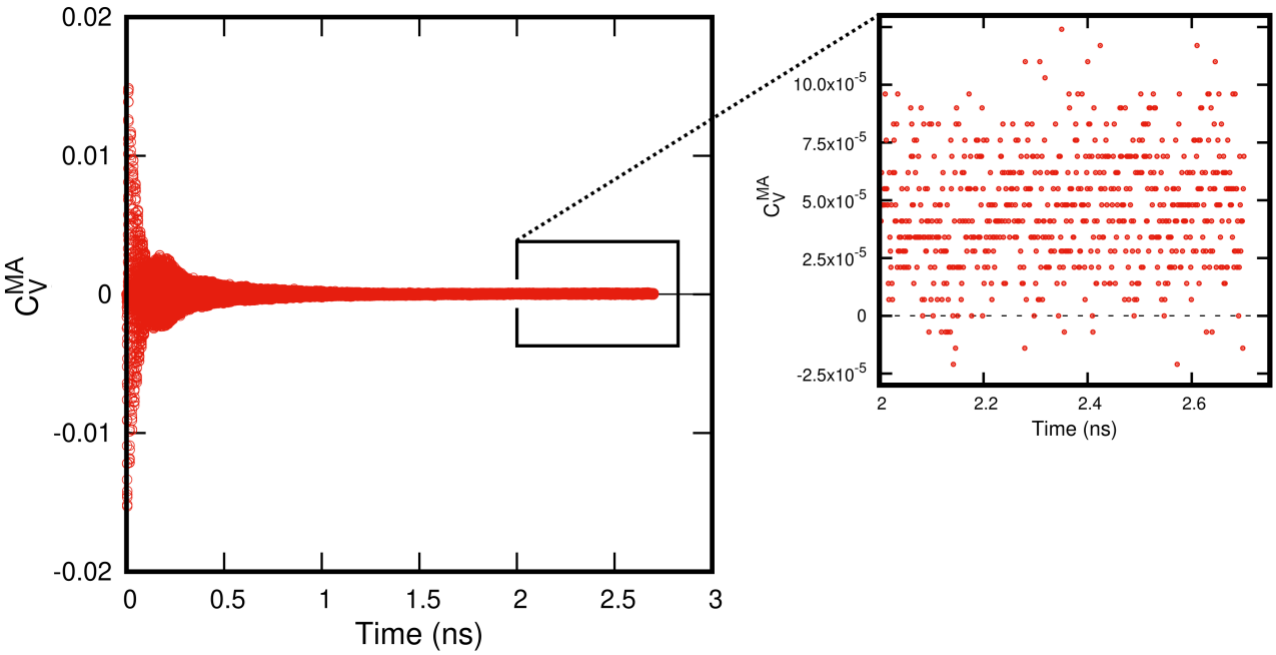

Figure S7. MLIP–MD equilibration of the larger 450000-atom Ti(001) surface-slab model at 1300 K used to determine the permanent equilibrium vacancy concentration c_V^{MA}. The relatively large temporal fluctuations in c_V^{MA} arise from the strong anharmonicity of bcc Ti: atoms in layers adjacent to the bulk region undergo substantial out-of-plane vibrations, causing some of them to be intermittently counted as bulk atoms.

S4. Mean vacancy concentrations from free energies of formation

The vacancy formation free energies G_V^f from Ref. [3] are characterized by symmetric standard deviations σ_G and therefore assumed to follow a Gaussian distribution reflecting their intrinsic spread at a given temperature. Assuming validity of the conventional thermodynamic relation for the dilute equilibrium vacancy concentration (**Eq. 3** of **main text**), the Gaussian distribution of G_V^f is mapped onto a lognormal distribution of vacancy concentrations. Introducing the log-space parameters $\mu_{ln} = -\frac{G_V^f}{k_B T}$ and $\sigma_{ln} = \frac{\sigma_G}{k_B T}$, the probability density of c_V^{TI} is given by the lognormal form $p(c_V^{TI}) = [\ 1 / (\ c_V\ \sigma_{ln} \sqrt{(2\pi)}\ ]\ \exp\{\ -[\ \ln(c_V^{TI}) - \mu_{ln}\ ]^2 / (2\ \sigma_{ln}^2)\}$. From this distribution, the median (geometric mean), arithmetic mean, and standard deviation of the vacancy concentration follow analytically. The median (geometric mean) concentration is $c_V^{TI\ median} = \exp[-G_V^f/(k_B T)]$, which coincides with **Eq. 3** of the **main text**. The arithmetic mean vacancy concentration with corresponding standard deviation are:

$$\langle c_V^{TI} \rangle = \exp\left(-\frac{G_V^f}{k_B T} + \frac{\sigma_G^2}{2\ (k_B T)^2} \right) \quad ; \quad \sigma_V = \langle c_V^{TI} \rangle \cdot \sqrt{\left\{ \exp\left[\frac{\sigma_G^2}{(k_B T)^2} \right] - 1 \right\}}. \qquad \textbf{(S1)}$$

Accordingly, the conventional expression yields the median of the vacancy concentration distribution, whereas the arithmetic mean is systematically larger due to the lognormal skewness.

S5. Steinhardt descriptor of atomic environments

To analyze the local structural environments arising from stress-activated transformations, we follow the SGMA methodology as used in Refs. [5, 6]. We construct a reference database using NVT sampling with the MLIP potentials of Al, Ti, and W of Ref. [7] using temperature ramps from 10 K to elevated temperatures for systems containing approximately 250 atoms. Ti systems in bcc, hcp, fcc, and ω phases are included as representative structures for comparison in the database.

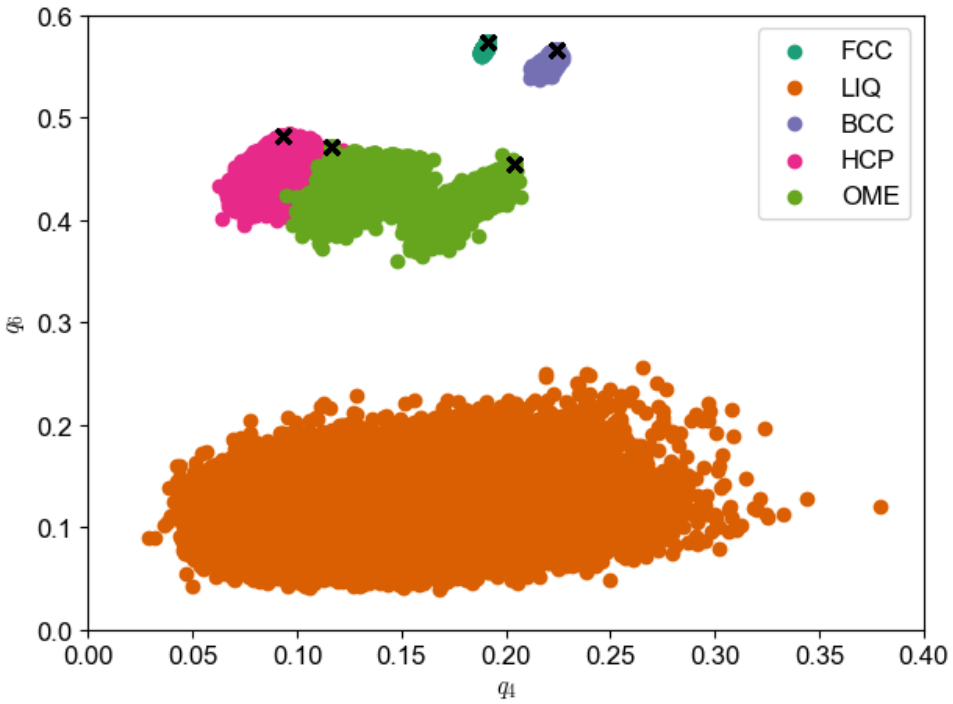

Figure S8. Scatter plot of the q_4 and q_6 values for the bcc, fcc, ω, and hcp structures in the database, where the crosses indicate q values for the perfect crystals. The snapshots are obtained from MLIP-MD simulations in the NVT ensemble for elements and temperatures at which the phase is expected to be stable. The liquid phase of ZnO [5] is included as a reference point for "disordered" structures and helps to avoid false positives in the prediction.

We then compute Voronoi-weighted Steinhardt order parameters, averaged over local neighborhoods, following Ref. [8], as implemented in the Python library Pyscal [9]. For each atom i, a complex vector q_{lm} is defined as:

$$q_{lm}(i)=\frac{1}{N_b(i)}\sum_{j=1}^{N_b(i)}\frac{A_{ij}}{A}Y_{lm}(\boldsymbol{r}_{ij}), \tag{S2}$$

where $N_b(i)$ is the number of neighbors of atom i, A_{ij} is the area of the Voronoi facet shared by atoms i and j, A is the total surface area of the Voronoi cell of atom i, and $\boldsymbol{r}_{ij}$ denotes the bond vector between atoms i and j. To improve crystal-phase recognition, the complex vector is averaged over the local neighborhood:

$$\bar{q}_{lm}(i)=\frac{1}{\widetilde{N_b}(i)}\sum_{k=0}^{\widetilde{N_b}(i)}q_{lm}(k), \tag{S3}$$

where the summation up to $\widetilde{N_b}$ includes atom i and all neighboring atoms N_b. The rotationally invariant Steinhardt order parameter q_l is then defined as:

$$q_l(i)=\sqrt{\frac{4\pi}{2l+1}\sum_{m=-l}^{l}\left|\bar{q}_{lm}(i)\right|^2}. \tag{S4}$$

The parameter q_6 is commonly used to distinguish between liquid-like and solid-like environments, while combined analysis of q_4 and q_6 enables identification of specific crystal structures. Steinhardt parameters of orders l = 2 through 8 are computed to ensure consistency across multiple symmetry descriptors.

After the per-atom structural information is calculated, we classify the atoms based on their local environment using a Gaussian Mixture Model, as implemented in the scikit-learn [10] library in Python. The Expectation-Minimization [11] algorithm is used iteratively to estimate the parameters of the model. The model is trained using full covariance matrices and 100 k-means initializations. We perform a grid search on the hyperparameters of the model and find that the optimal number of

Gaussian clusters is K=16. Once the Gaussian clusters are fitted, we compare them to the structures in the database to assign labels to each cluster. The probability of each atom to belong to a class ω_k can then be calculated using its descriptor vector $\boldsymbol{x}_i$ (built using the Steinhardt parameters) and the Maximum Likelihood Classifier as

$$p(\omega_k|\boldsymbol{x}_i) = \frac{\alpha_k \mathcal{N}(\boldsymbol{x}_i|\boldsymbol{m}_k,\boldsymbol{C}_k)}{\sum_{j=1}^{K} \alpha_j \mathcal{N}\left(\boldsymbol{x}_i\middle|\boldsymbol{m}_j,\boldsymbol{C}_j\right)}, \quad \textbf{(S5)}$$

where "$\mathcal{N}$" is a normal distribution, α_k are mixture proportions and $\boldsymbol{m}_k$ and $\boldsymbol{C}_k$ are the mean vector and the covariance matrix of each Gaussian component ω_k. The mixture proportions α_k satisfy the conditions $0 \leq \alpha_k \leq 1$ and $\sum_{k=1}^{K} \alpha_k = 1$. In this way we can classify atoms based on the highest probability that they have of being in hcp, bcc, fcc, or omega phases. This facilitates an understanding of phase changes present during a simulation (**Fig. S8**).

S6. Description of AIMD videos

The videos show ~25 ps of AIMD dynamics in pure metals modeled by defect-free 9×9×9 bcc supercells (1458 atoms) at simulation temperatures of ~0.93 $T_m^{expt.}$. To reduce vibrational noise and make diffusion pathways easier to visualize, the atomic trajectories are averaged over 1 ps.

Video 1: bcc Sc; Video 2: bcc Ti; Video 3: bcc Zr; Video 4: bcc Hf; Video 5: bcc V. No video is shown for bcc Mo, since no migration event occurs over the simulated time, as in bcc V.

[1] D.G. Sangiovanni, D. Edström, L. Hultman, I. Petrov, J.E. Greene, V. Chirita, Ti adatom diffusion on TiN(001): *Ab initio* and classical molecular dynamics simulations, Surface Science 627 (2014) 34.

[2] H. Wang, Y. Wu, Direct monitoring of vacancy thermal equilibration, Journal of Physical Chemistry Letters 16 (2025) 6608.

[3] J.H. Jung, A. Forslund, P. Srinivasan, B. Grabowski, Dynamically stabilized phases with full *ab initio* accuracy: Thermodynamics of Ti, Zr, Hf with a focus on the hcp-bcc transition, Physical Review B 108 (2023) 184107.

[4] X. Zhang, S. Divinski, B. Grabowski, Ab initio machine-learning unveils strong anharmonicity in non-Arrhenius self-diffusion of tungsten, Nature Communications **16** (2025) 394.

[5] J. Furstoss, C.R. Salazar, P. Carrez, P. Hirel, J. Lam, All-around local structure classification with supervised learning: The example of crystal phases and dislocations in complex oxides, Computer Physics Communications 309 (2025) 109480.

[6] C.R. Salazar, A.K. Ammothum Kandy, J. Furstoss, Q. Gromoff, J. Goniakowski, J. Lam, Competing nucleation pathways in nanocrystal formation, npj Computational Materials 10 (2024) 199.

[7] K. Song, R. Zhao, J. Liu, Y. Wang, E. Lindgren, Y. Wang, S. Chen, K. Xu, T. Liang, P. Ying, General-purpose machine-learned potential for 16 elemental metals and their alloys, Nature Communications 15 (2024) 10208.

[8] W. Mickel, S.C. Kapfer, G.E. Schröder-Turk, K. Mecke, Shortcomings of the bond orientational order parameters for the analysis of disordered particulate matter, The Journal of Chemical Physics 138 (2013) 044501.

[9] S. Menon, G.D. Leines, J. Rogal, pyscal: A python module for structural analysis of atomic environments, Journal of Open Source Software 4 (2019) 1824.

[10] F. Pedregosa, G. Varoquaux, A. Gramfort, V. Michel, B. Thirion, O. Grisel, M. Blondel, P. Prettenhofer, R. Weiss, V. Dubourg, Scikit-learn: Machine learning in Python, the Journal of Machine Learning Research 12 (2011) 2825.

[11] A.P. Dempster, N.M. Laird, D.B. Rubin, Maximum likelihood from incomplete data via the EM algorithm, Journal of the royal statistical society: series B (methodological) 39 (1977) 1.